



HAL
open science

Influence of Strong Confinement on the Structure and Dynamics of Liquids: a Study of the Clay/Water Interface Exploiting ^2H NMR Spectroscopy and Spin-Locking Relaxometry

Patrice Porion, Anne-Marie Faugère, Anne-Laure Rollet, Emmanuelle Dubois, Virginie Marry, Laurent Michot, Alfred Delville

► To cite this version:

Patrice Porion, Anne-Marie Faugère, Anne-Laure Rollet, Emmanuelle Dubois, Virginie Marry, et al.. Influence of Strong Confinement on the Structure and Dynamics of Liquids: a Study of the Clay/Water Interface Exploiting ^2H NMR Spectroscopy and Spin-Locking Relaxometry. *Journal of Physical Chemistry C*, 2018, 122 (29), pp.16830-16841. 10.1021/acs.jpcc.8b05089 . hal-02383136

HAL Id: hal-02383136

<https://hal.science/hal-02383136>

Submitted on 10 Dec 2021

HAL is a multi-disciplinary open access archive for the deposit and dissemination of scientific research documents, whether they are published or not. The documents may come from teaching and research institutions in France or abroad, or from public or private research centers.

L'archive ouverte pluridisciplinaire **HAL**, est destinée au dépôt et à la diffusion de documents scientifiques de niveau recherche, publiés ou non, émanant des établissements d'enseignement et de recherche français ou étrangers, des laboratoires publics ou privés.

This document is confidential and is proprietary to the American Chemical Society and its authors. Do not copy or disclose without written permission. If you have received this item in error, notify the sender and delete all copies.

Influence of Strong Confinement on the Structure and Dynamics of Liquids: A Study of the Clay/Water Interface Exploiting ^2H NMR Spectroscopy and Spin-Locking Relaxometry

Journal:	<i>The Journal of Physical Chemistry</i>
Manuscript ID	jp-2018-050893.R1
Manuscript Type:	Article
Date Submitted by the Author:	n/a
Complete List of Authors:	Porion, Patrice; CNRS-Universite d'Orleans, Interfaces, Confinement, Materiaux et Nanostructures (ICMN) Faugère, Anne Marie; CNRS-Universite d'Orleans, Centre de Recherche sur la Matiere Div. Rollet, Anne-Laure; cnrs, PECSA Dubois, Emmanuelle; Université Pierre et Marie Curie, Laboratoire PHENIX Marry, Virginie; UPMC, Michot, Laurent; PhENix(Physicochimie des Electrolytes et Nanosystèmes Interfaciaux), UMR 8234 - CNRS - UPMC Delville, Alfred; CNRS, CRMD

SCHOLARONE™
Manuscripts

1
2
3
4
5
6
7
8
9
10
11
12
13
14
15
16
17
18
19
20
21
22
23
24
25
26
27
28
29
30
31
32
33
34
35
36
37
38
39
40
41
42
43
44
45
46
47
48
49
50
51
52
53
54
55
56
57
58
59
60

**Influence of Strong Confinement on the Structure and Dynamics of
Liquids: A Study of the Clay/Water Interface Exploiting ^2H NMR
Spectroscopy and Spin-Locking Relaxometry**

Patrice Porion^{a,*}, Anne Marie Faugère^a, Anne-Laure Rollet^b, Emmanuelle Dubois^b,
Virginie Marry^b, Laurent J. Michot^b, and Alfred Delville^{a,*}

^a Interfaces, Confinement, Matériaux et Nanostructures, ICMN, UMR 7374,
CNRS - Université d'Orléans, 45071 Orléans Cedex 02, France

^b Physicochimie des Electrolytes et Nanosystèmes Interfaciaux, PHENIX, UMR 8234,
CNRS - Sorbonne Université, 4 place Jussieu, 75252 Paris Cedex 5, France

***Corresponding authors:**

E-mail: delville@cnrs-orleans.fr (A.D.) and porion@cnrs-orleans.fr (P.P.).

Abstract

^2H NMR spectroscopy, multi-quantum relaxation and spin-locking relaxometry are used to investigate the structural and dynamical properties of water molecules confined within dense sediments of synthetic fluoro-hectorite. As shown by the large residual splitting of the ^2H NMR resonance line, water molecules confined in the interlamellar space of the clay are strongly oriented at contact with the fluorinated basal surface of the clay. Multi-quantum relaxation measurements are used to identify and quantify the contributions of the quadrupolar and hetero-nuclear dipolar couplings monitoring the NMR relaxation of the confined water molecules. Finally, the average residence time of the water molecules confined within the interlamellar space of the clay platelets is quantified by a detailed analysis of ^2H spin-locking relaxometry measurements. Thanks to the significant contributions of both quadrupolar and hetero-nuclear dipolar relaxation mechanisms, ^2H spin-locking relaxation measurements probe a broad dynamical range, by sampling angular velocities ranging between 10^2 and 3×10^5 rad/s.

I. Introduction

In the last decades, solid/liquid interfaces were the subject of numerous experimental^{1,2} and theoretical^{3,4} studies since confinement greatly modifies the structural and dynamical properties⁵⁻¹³ of fluids. In that context, clay/water interfacial systems were frequently investigated for two reasons. Firstly, from a theoretical point of view, clay platelets are ideal models for studying solid/liquid interfaces since they have an atomically smooth surface with well-characterized structure and atomic composition. Secondly, natural and synthetic clays are employed in many industrial applications (drilling, waste storing, ionic exchange, heterogeneous catalysis) exploiting their various physico-chemical properties¹⁴ (swelling, thixotropy, large specific surface area and surface charge density, adsorbing power, surface acidity). Monitoring and predicting the mobility of confined molecules in the porous network of clay aggregates is thus of prime importance for optimizing a large class of such industrial applications. As a consequence, numerous experimental studies have been performed to determine the mobility of confined fluids over a broad range of diffusing time. At short time-scale (between 10^{-12} and 10^{-7} seconds), Inelastic¹⁵⁻¹⁸ and Quasi-Elastic^{13,19,20} Neutron Scattering were frequently used to obtain information on the local mobility of the confined fluids. By contrast, the long-time mobility (above milli-seconds) of fluids is generally probed by using pulsed gradient spin echo (PGSE) NMR spectroscopy^{21,22}. But under confinement, the large enhancement of the NMR relaxation rates^{23,24} generally prohibits the use of PGSE NMR spectroscopy. Recent ^2H NMR relaxations measurements²⁵ have illustrated the large enhancement of deuterium NMR relaxation rate of heavy water confined within dense clay sediments. In that context, NMR relaxometry²⁶ provides an interesting alternative way to obtain information on the long-time mobility of confined fluids. For that purpose, we performed ^2H spin-locking relaxometry measurements, because a broad frequency domain may be probed by quadrupolar nuclei (with spin $I > 1/2$) under

1
2
3
4 confinement²⁶⁻³⁰. By contrast with spin-locking NMR relaxometry²⁶⁻³⁰, both PGSE-NMR
5
6 spectroscopy^{21,22} and field-cycling NMR relaxometry^{22,31} require incompressible time-delays
7
8 necessary either to create stable magnetic field gradients, in the case of PGSE, or switch the
9
10 strength of the static magnetic field, in the case of field-cycling relaxometry. These inherent
11
12 time-delays strongly limit the applicability of these experimental procedures for investigating
13
14 the dynamical behavior of strongly confined fluids because of the enhancement of their NMR
15
16 relaxation rates induced by confinement^{23,24}.
17
18
19
20

21
22 In that study we selected to use a synthetic clay sample (fluoro-hectorite) in order to
23
24 avoid the tremendous enhancement of the NMR relaxation induced by paramagnetic
25
26 impurities generally present in natural clay^{26,27}. Furthermore, substitution of the structural
27
28 hydroxides at the clay surface by fluorine atoms greatly simplifies the interpretation of ²H
29
30 NMR spectra since all the deuterium atoms detected by ²H NMR spectroscopy pertain to the
31
32 added water molecules. The ²H NMR spectra are first recorded to quantify the degree of
33
34 ordering of confined water molecules. The influence of surface hydrophobicity on the
35
36 organization of confined water molecules is clearly demonstrated by comparing the measured
37
38 residual quadrupolar splitting to values previously reported, under the same experimental
39
40 conditions, for classical hectorite with hydroxides in the clay layer. Multi-quanta ²H
41
42 relaxation measurements are performed for various orientations of the clay film by reference
43
44 with the static magnetic field \mathbf{B}_0 in order to quantify the contributions of the quadrupolar and
45
46 heteronuclear dipolar couplings responsible for the relaxation of confined water molecules.
47
48 Finally, spin-locking relaxometry measurements are performed to determine the frequency
49
50 variation of the NMR relaxation rates. This dynamical information gives direct access to the
51
52 average residence time of the water molecules confined in the interlamellar space of clay
53
54 platelets. Such analysis of the ²H NMR relaxation measurements requires a complete analysis
55
56
57
58
59
60

1
2
3
4 of the time evolution of the components of the spin=1 nuclei under the influence of the NMR
5
6 relaxation mechanisms in addition to the residual quadrupolar splitting and the irradiation
7
8 pulses.
9

10 11 12 **II. Materials and Methods**

13 14 15 **II.1. Sample Preparation**

16
17
18 Figure 1

19
20
21
22 The clay sample used in that study is a synthetic hectorite with the general formula
23
24 $\text{Si}_8(\text{Mg}_{5.2}\text{Li}_{0.8})\text{O}_{20}\text{F}_4\text{Cs}_{0.8}$. It results from the sandwiching of one octahedral layer of
25
26 magnesium oxides between two tetrahedral layers of silica¹⁴. The hydroxide atoms generally
27
28 located within the hexagonal cavity of the two silica layers are replaced by fluorine atoms,
29
30 strongly modifying the water affinity for the clay surface^{32,33}. The negative charge of the clay
31
32 platelets results from substitutions, in the octahedral layer, of some magnesium by lithium.
33
34 These negative charges are neutralized by cesium cations localized in the interlamellar space
35
36 between clay platelets. As determined by transmission electronic microscope³⁰, the average
37
38 size of the individual clay platelet is $(0.3 \pm 0.1) \mu\text{m}$. More details on the synthesis and
39
40 characterization of that clay sample are given in the literature³⁴. Oriented clay membranes
41
42 (10 μm thickness) were prepared by sedimentation of a dilute dispersion ($\sim 20 \text{ g/L}$) and air-
43
44 dried on a flat surface. Successive deposits were stacked to form a macroscopic film with a
45
46 3 mm thickness³⁰. As a consequence, the macroscopic clay film exhibits multi-scale structure
47
48 since it results from the superposition of numerous individual membranes each composed
49
50 from partially oriented clay aggregates (see Figure 1). As determined by X-ray diffraction³²,
51
52 the thickness of these clay aggregates roughly corresponds to 20 clay platelets. The
53
54 macroscopic clay film was equilibrated with bulk heavy water at a relative humidity close
55
56
57
58
59
60

1
2
3
4 to 97%, leading to the formation of one hydration layer³³. As measured by water
5
6 adsorption/desorption isotherms³⁰, the total water content of this Cs⁺/fluorohectorite sample is
7
8 3.9 mmol of water per gram of dry clay, corresponding roughly to four water molecules per
9
10 cesium cation. Obviously, the first hydration layer of cesium cation immersed in bulk water
11
12 contains more than four water molecules³⁵. In our case, strong confinement results from the
13
14 formation of a single hydration layer³³. As a consequence, ions and water molecules are
15
16 located in the equatorial plane at the center of the interlamellar space between the clay
17
18 platelets, thus restricting hydration of the confined counterions. A fragment of the clay film
19
20 (20 mm length, 3 mm width) is cut and inserted in a glass tube fitting the inner cavity of the
21
22 homemade NMR detection coil. To avoid clay desiccation during NMR experiments, a
23
24 droplet of heavy water is deposited in the sealing cap of the glass tube, *i.e.* at a position as far
25
26 as possible from the NMR detection coil.
27
28
29
30
31
32

33 II.2. NMR Measurements

34 35 36 Figure 2

37
38
39 ²H NMR spectra and relaxation measurements of confined heavy water were recorded
40
41 on a DSX360 Bruker spectrometer operating at a static magnetic field \mathbf{B}_0 of 8.465 T. On this
42
43 spectrometer, typical pulse duration for the total inversion of the longitudinal magnetization is
44
45 equal to 9 μ s by using a homemade detection coil. Spectra were recorded using a fast
46
47 acquisition mode with spectral width of 1 MHz with a numerical spectral resolution of 125 Hz.
48
49 The spectra and relaxation measurements were performed at various orientations of the clay
50
51 film as described by the β^{LF} Euler angle between the direction of the static magnetic field \mathbf{B}_0
52
53 and the macroscopic film director \vec{n}^F (see Figure 2).
54
55
56
57
58
59
60

1
2
3
4 A complete basis set^{36,37}, with eight independent operators is required to fully describe
5
6 the time evolution of the magnetization of spin I=1 nuclei under the influence of pulse
7
8 sequences, residual quadrupolar coupling and relaxation mechanisms (see the Supporting
9
10 Information (SI)). A possible basis set is given by the irreducible tensor operators^{36,37} [T_{10}^{IR} ,
11
12 $T_{11}^{IR}(a,s)$, T_{20}^{IR} , $T_{21}^{IR}(a,s)$ and $T_{22}^{IR}(a,s)$] also called coherences. The first three coherences
13
14 describes the components of the longitudinal T_{10}^{IR} and transverse $T_{11}^{IR}(a,s)$ magnetization,
15
16 while the next five coherences are required to describe quadrupolar coupling. Each of these
17
18 coherences have their own time evolution which may be independently measured by multi-
19
20 quanta filtering to fully characterize the contributions of the competing quadrupolar and
21
22 heteronuclear dipolar relaxation mechanisms²⁵⁻²⁹ (see the SI).
23
24
25
26
27
28
29

30 II.3. Numerical simulations

31
32 The LAMMPS package³⁸ (<http://lammps.sandia.gov>) was used to perform numerical
33
34 simulations of Molecular Dynamics (MD) of the clay/water interface by exploiting the
35
36 classical CLAYFF force field³⁹ adapted to fluoro-hectorite²⁰. The interactions between water
37
38 molecules are described by using the TIP4P/2005 model of bulk water⁴⁰. The general formula
39
40 of the fluoro-hectorite unit cell is $\text{Cs}_{0.8}\text{Si}_8(\text{Mg}_{5.2}\text{Li}_{0.8})\text{O}_{20}\text{F}_4$. The simulation cell contains two
41
42 clay lamellae, each composed from 40 unit cells. The number of confined water molecules (4
43
44 H_2O per Cs cation) was selected to reproduce the water uptake of fluoro-hectorite³⁰
45
46 neutralized by Cs^+ cations. The interlamellar separation between the two clay lamellae is also
47
48 fixed at 12.4 \AA ³². MD simulations were performed in the NVT ensemble to evaluate the
49
50 trajectories during 5 ns. The water mobility in the direction parallel to the clay surface is
51
52 evaluated from the asymptotic slope of the corresponding mean squared displacements.
53
54
55
56
57
58
59
60

III. Results and Discussion

III.1. ^2H NMR Spectra

Figure 3

As displayed in Figure 3, ^2H NMR spectra of the hydrated clay sediment exhibit the coexistence of two spin populations characterized by a broad doublet and a thin central resonance line corresponding to confined and bulk water, respectively. As previously detected for clay sediments²⁵⁻²⁹, the quadrupolar splitting ν_Q^{obs} of confined water molecules results from specific orientation of their OD director by reference to the director, noted \vec{n}^F , pertaining to their confining clay platelets, in agreement with results obtained by numerical simulations²⁵⁻²⁹. As a consequence, the detected quadrupolar splitting ν_Q^{obs} varies as a function of the orientation β^{LF} , into the static magnetic field \mathbf{B}_0 , of the macroscopic clay film according to the relationship (see the SI):

$$\nu_Q^{obs}(\beta^{LF}) = \left| \frac{3 \cos^2(\beta^{LF}) - 1}{2} \right| \times \left\langle \frac{3 \cos^2(\beta^{FD}) - 1}{2} \right\rangle \times 210 \text{ kHz} \quad (1)$$

where the first second order Legendre polynomial $P_2(\cos(\beta^{LF})) = 0.5(3 \cos^2(\beta^{LF}) - 1)$ describes the orientation of the macroscopic clay film into the static magnetic field characterized by the β^{LF} Euler angle (see Section II.2) and the second Legendre polynomial $P_2(\cos(\beta^{FD}))$, into the bracket, describes the average orientation of the OD directors of the confined water molecules defined by their β^{FD} Euler angle by reference with the normal to their confining clay platelets (see the SI). Finally, the quadrupolar coupling constant (QCC) of deuterium (^2H) in heavy water⁴¹ is equal to 210 kHz. In addition to confined water, bulk water

1
2
3
4 molecules are localized either in the cap of the glass tube (see Section II.1) or within the
5
6 micro-porosity between the aggregates of clay platelets. By contrast with confined water
7
8 molecules, bulk water molecules are randomly oriented and exchange slowly, at the NMR
9
10 time-scale⁴², with the confined water molecules leading to a thin central resonance line fully
11
12 independent of the film orientation within the static magnetic field \mathbf{B}_0 . By contrast with field-
13
14 cycling NMR relaxometry, the stability and homogeneity of the static magnetic field induced
15
16 by the supraconducting magnet (see Section II.2) lead to a experimental spectral resolution of
17
18 the ^2H NMR spectra of the order of a few 100 Hz, *i.e.* largely sufficient to distinguish the
19
20 contributions of the confined and bulk water molecules to the total detected magnetization
21
22 (see Figure 2).
23
24
25
26
27
28

29 As displayed in Figure 3, the maximum residual splitting (57 ± 3) kHz detected for a
30
31 parallel alignment between the film director \vec{n}^F and the static magnetic field \mathbf{B}_0 is much
32
33 larger than values previously measured at room temperature for heavy water confined within a
34
35 large class of clays^{25-29,41}. One may be tempted to attribute this surprisingly large splitting to
36
37 the exchange between deuterium atoms of confined heavy water and protons from the clay
38
39 structure. Such interpretation is not plausible since hydroxylates on the basal surface of the
40
41 clay platelet are totally replaced by fluorine atoms (see Section II.1). Furthermore, the total
42
43 number of hydroxylates localized on the edge surface of clay platelets is two orders of
44
45 magnitude smaller than the number of deuterium atoms pertaining to confined water
46
47 molecules. As a consequence, the large residual splitting reported here is the fingerprint of a
48
49 strong organization of confined water molecules since the corresponding order parameter (*i.e.*
50
51 the averaged Legendre polynomial of Eq. 2) must be equal to (0.36 ± 0.02). By contrast,
52
53 previous ^2H NMR measurements lead to much smaller order parameter (0.10 ± 0.01) for
54
55 water molecules confined within **hydroxylated hectorite** neutralized by **sodium** counterions
56
57
58
59
60

1
2
3
4 under the similar hydration conditions^{28,41}. By contrast, the order parameter of water
5
6 molecules confined within the same **hydroxylated hectorite** increases slightly to 0.15 when
7
8 **sodium** counterions are replaced by **cesium**⁴¹. As a consequence, the high value reported here
9
10 for the order parameter of confined water molecules is not induced by the chemical nature of
11
12 the neutralizing monovalent cation but illustrates the large influence of the fluorine atoms
13
14 located at the center of the ditrigonal cavity on the organization of the water molecules
15
16 confined within the interlamellar space between the clay platelets.
17
18
19
20

21
22 The residual order parameter evaluated by MD simulations, $\langle P_2(\cos(\beta^{FD})) \rangle \approx 0.204$, is
23
24 significantly smaller than the experimental value, restricting the validity of the potentials used
25
26 here to describe the hydration of fluoro-hectorite neutralized by Cesium counterions. Despite
27
28 the large deficiency of the model, the numerical data may nevertheless be used in some
29
30 qualitative way to illustrate the organization of the confined water molecules. As displayed in
31
32 Figure 4a, the oxygen atoms of the water molecules are predominantly localized in the
33
34 equatorial plane of the clay interface. Three peaks are easily identified in the concentration
35
36 profile of the hydrogen atoms, suggesting a specific orientation of the confined water
37
38 molecule characterized by one *OD* director pointing along the normal to the clay platelets
39
40 (noted \vec{n}^F). Figure 4b validates that analysis by exhibiting a bimodal distribution of the *OD*
41
42 directors by reference to \vec{n}^F : in addition to a broad distribution around 70°
43
44 $\{ 69.5^\circ = \arccos(0.35) \}$, an intense sharp peak appears at 0° corresponding to water molecules
45
46 pointing one *OD* director parallel to \vec{n}^F the normal to the clay platelet. Further information
47
48 on the water orientation in the interlamellar space are given by the distributions of the
49
50 directors describing the water dipole and the normal to the *DOD* plane of the water
51
52 molecules by reference to \vec{n}^F . As illustrated by their broad distribution in Figure 4b, the
53
54 directors perpendicular to the *DOD* plane are not totally perpendicular to the normal \vec{n}^F to
55
56
57
58
59
60

1
2
3
4 the clay platelet. As a consequence, the orientation of the water dipole by reference to the
5
6 normal \vec{n}^F exhibits a broad distribution around 60° $\{58.7^\circ = \arccos(0.52)\}$ while an angle of
7
8 52.26° should occur for water molecules with an *OD* director perfectly pointing to the clay
9
10 surface with its *DOD* plane perpendicular to the clay surface. The degree of ordering of the
11
12 confined water molecule is further illustrated in Figure 5, where the white vertical and
13
14 horizontal lines correspond to the orientation of the perfectly oriented water molecule
15
16 mentioned above.
17
18
19
20

21
22 Figures 4a and 4b
23

24
25 Figure 5
26
27
28

29 III.2. ^2H Multi-Quanta NMR Relaxation Measurements

30
31
32 Figure 6
33
34
35

36 The relaxation of the T_{10}^{IR} coherence (also called longitudinal relaxation rate $R_1 \equiv R_{10}$)
37
38 of bulk water present in the sample was measured by using a classical saturation-recovery
39
40 pulse sequence⁴³. The average longitudinal relaxation rate measured here for bulk water
41
42 ($R_{10} = 25 \pm 5 \text{ s}^{-1}$) is one order of magnitude larger than the longitudinal relaxation rate
43
44 previously reported for pure D_2O ($R_{10} = 2.5 \pm 0.1 \text{ s}^{-1}$)⁴⁴. In order to selectively measure the
45
46 longitudinal relaxation rate of confined water molecules we used a saturation-recovery pulse
47
48 sequence followed by a double-quanta filtering (see Figure 6a). As displayed in Figure 6a, the
49
50 duration of the first detection pulse was selected to optimize the transfer of magnetization
51
52 between the T_{10}^{IR} and $T_{22}^{IR}(a)$ coherences, see Eq. S5d in the SI. In the same manner, the
53
54 duration of the second detection pulse optimizes the $T_{22}^{IR}(a)$ to $T_{11}^{IR}(s)$ transfer of coherence
55
56
57
58
59
60

(see Eq. A5b in the SI). As previously reported for other clay/water interfaces²⁵⁻²⁹, the longitudinal relaxation rate of confined water molecules ($R_{10} = 130 \pm 30 \text{ s}^{-1}$) is significantly enhanced by reference with the relaxation rate of pure water ($R_{10} = 2.5 \pm 0.1 \text{ s}^{-1}$)⁴⁴.

By contrast with bulk liquids, the relaxation rates of liquids confined within 2D interfacial systems vary as a function of the orientation of the interface by reference with the direction of the static magnetic field \mathbf{B}_0 ²⁵⁻²⁹. As a consequence, it becomes crucial to extract from the angular variation of the apparent relaxation rates the contributions of the various relaxation mechanisms to the intrinsic relaxation rates evaluated in the frame of the confining lamellae. This may be performed by using the Wigner rotation matrices⁴⁵ that relates the apparent spectral densities $J_m^{X,app}(\omega)$ measured in the laboratory frame to the intrinsic spectral density $J_m^{X,int}(\omega)$ evaluated in the frame attached to the clay film, where X stems for the relaxation mechanisms $X \in \{Q, D\}$ and $m \in \{0, 1, 2\}$, see Eqs S9 and S12 in the SI:

$$J_0^{X,app}(\beta^{LF}, \omega) = \frac{1}{4}(1 - 3\cos^2\beta^{LF})^2 J_0^{X,int}(\omega) + \frac{3}{4}(\sin 2\beta^{LF})^2 J_1^{X,int}(\omega) + \frac{3}{4}(\sin\beta^{LF})^4 J_2^{X,int}(\omega) \quad (2a)$$

$$J_1^{X,app}(\beta^{LF}, \omega) = \frac{3}{2}\cos^2\beta^{LF}\sin^2\beta^{LF} J_0^{X,int}(\omega) + \frac{1}{2}(1 - 3\cos^2\beta^{LF} + 4\cos^4\beta^{LF}) J_1^{X,int}(\omega) + \frac{1}{2}(1 - \cos^4\beta^{LF}) J_2^{X,int}(\omega) \quad (2b)$$

$$J_2^{X,app}(\beta^{LF}, \omega) = \frac{3}{8}(1 - \cos^2\beta^{LF})^2 J_0^{X,int}(\omega) + \frac{1}{2}(1 - \cos^4\beta^{LF}) J_1^{X,int}(\omega) + \frac{1}{8}(1 + 6\cos^2\beta^{LF} + \cos^4\beta^{LF}) J_2^{X,int}(\omega) \quad (2c)$$

1
2
3
4 The relaxation of the $T_{21}^{IR}(a)$ and $T_{22}^{IR}(a)$ coherences are thus measured as a function
5
6 of the orientation of the macroscopic clay film into the static magnetic field \mathbf{B}_0 probed by the
7
8 Euler angle β^{LF} , in order to extract the relative contributions of the quadrupolar and
9
10 heteronuclear dipolar relaxation mechanisms (see the SI). These relaxation measurements are
11
12 again performed by using an initial saturation pulses train followed by multi-quanta filtering
13
14 (see Figure 6b-c). As detailed in Eqs S6b-c in the SI, the angular velocities k_2 and k_3 ,
15
16 monitoring the time evolution of the various coherences (see Eqs.S5b-d in the SI) vary as a
17
18 function of the residual quadrupolar coupling ω_Q . Because of the large residual quadrupolar
19
20 coupling detected here, the durations of the filtering pulses are thus specifically selected for
21
22 each orientation of the clay sample according to the set of Eqs S5b-d (see the SI) in order to
23
24 optimize the coherence transfers implied in these relaxation measurements. These settings of
25
26 the pulse durations may reasonably neglect the contribution from the NMR relaxation
27
28 mechanisms to the time evolution of the coherences since the pulse durations (typically a
29
30 few μs) are short enough compared to the NMR relaxation times. In order to remove the
31
32 contribution from the central resonance line, our analysis focuses on the frequency domains
33
34 covered by the satellite. Figures 7 and 8 illustrate typical spectra measured during the time
35
36 evolution of $T_{21}^{IR}(a)$ and $T_{22}^{IR}(a)$ coherences for an orientation of the macroscopic film
37
38 director either parallel ($\beta^{LF} = 0^\circ$) or perpendicular ($\beta^{LF} = 90^\circ$) to the static magnetic field \mathbf{B}_0 ,
39
40 respectively.
41
42
43
44
45
46
47
48
49
50

51 Figure 7 and Figure 8

52
53
54
55 During the time evolution of the $T_{21}^{IR}(a)$ coherence (see Figure 7), we expected to
56
57 detect a single resonance line occurring at the characteristic residual quadrupolar splitting
58
59
60

1
2
3
4 given by Eq. 1 (*i.e.* 57000 Hz at $\beta^{LF}=0^\circ$ and 27000 Hz at $\beta^{LF}=90^\circ$). By contrast, the stacked
5
6 spectra displayed in Figure 7 clearly exhibit curved resonance bands whose number increases
7
8 as a function of the time delay. By using the set of Eqs S8 and S11 in the SI, we simulate the
9
10 time evolution of the various coherences during each elementary step of the pulse sequence
11
12 displayed in Figure 6b. It then becomes possible to reproduce the structure of the stacked
13
14 spectra (see Figure 7) by including in our numerical model a Gaussian distribution of the
15
16 orientation of the individual clay directors by reference to the director of the macroscopic film.
17
18 The same approach was used to simultaneously analyze the time evolution of the $T_{22}^{IR}(a)$
19
20 coherence (see Figure 8) measured by the pulse sequence displayed in Figure 6c.
21
22
23
24
25
26

27 The whole set of experimental data displayed in Figures 7 and 8 is fairly well
28
29 reproduced by using a limited number of parameters quantifying the maximum residual
30
31 splitting corresponding to a parallel orientation of the clay film $\nu_Q^{\max} = (57 \pm 2)$ kHz , the
32
33 intrinsic contributions of the quadrupolar (see Eq 2a with $X = Q$): $J_0^{Q,int}(0) = (550 \pm 50)$ s⁻¹ ,
34
35 $J_1^{Q,int}(0) = (5000 \pm 1000)$ s⁻¹ and $J_2^{Q,int}(0) = (120 \pm 20)$ s⁻¹ , and dipolar (see Eq 2a with
36
37 $X = D$): $J_0^{D,int}(0) = J_1^{D,int}(0) = (2700 \pm 300)$ s⁻¹ and $J_2^{D,int}(0) = (1700 \pm 300)$ s⁻¹ relaxation
38
39 mechanisms, in addition to the width of the Gaussian distribution of the individual clay
40
41 directors \vec{n}^F in the macroscopic film with $\sigma_\beta = (17 \pm 3)^\circ$. By contrast with bulk liquids, both
42
43 sets of intrinsic contributions to the quadrupolar $J_m^{Q,int}(0)$ with $m \in \{0, 1, 2\}$ and heteronuclear
44
45 dipolar $J_m^{D,int}(0)$ with $m \in \{0, 1, 2\}$ relaxation mechanisms vary as a function of the index m ,
46
47 leading to angular dependent transverse relaxation rates (see Eqs 2a). That behavior is
48
49 induced by the water confinement within the clay interlamellar space, breaking down the
50
51 isotropy of the distribution of the Euler angles (θ^{LW}, ϕ^{LW}) characterizing the orientation of the
52
53
54
55
56
57
58
59
60

1
2
3
4 *OD* directors of the water molecules into the static magnetic field \mathbf{B}_0 . As a consequence, in
5
6 the case of confined water molecules the average values of the second order spherical
7
8 harmonics $Y_{2,m}(\theta^{LW}, \phi^{LW})$ with $m \in \{0,1,2\}$ implied in the derivation of the quadripolar and
9
10 dipolar Hamiltonians (see the SI) differ significantly. In that context, the significant
11
12 enhancement of the $J_1^{Q,int}(0)$ contribution induces a corresponding increase of the transverse
13
14 relaxation rate for orientations of the film director close to $\beta^{LF} = 45^\circ$ by reference with the
15
16 static magnetic field \mathbf{B}_0 . That specific angle corresponds indeed to the maximum value of the
17
18 $(\sin 2\beta^{LF})^2$ function weighting the contribution of $J_1^{Q,int}(0)$ in the derivation of the apparent
19
20 transverse relaxation rate (see Eq. 2a). In the same manner, the smallest transverse relaxation
21
22 rate is always detected for a perpendicular orientation of the film director (*i.e.* $\beta^{LF} = 90^\circ$) by
23
24 reference with the direction of the static magnetic field \mathbf{B}_0 ²⁵⁻²⁹.

33 34 III.3. ²H NMR Spin-Locking Relaxometry

35 36 37 Figure 9

38
39
40 As a consequence, spin-locking relaxation measurements were performed for a
41
42 perpendicular orientation of the film director, *i.e.* $\beta^{LF} = 90^\circ$, in order to optimize the
43
44 signal/noise ratio of the doublet describing the dynamical properties of confined water
45
46 molecules. Figure 9 illustrates the pulse sequences used for these spin-locking relaxation
47
48 measurements: after a first excitation pulse, the irradiation power is applied for variable
49
50 evolution time before acquisition of the transverse magnetization. In the so-called T_{2p} spin-
51
52 locking relaxation measurement, both excitation and irradiation pulses have the same phase⁴⁶
53
54 while for T_{1p} spin-locking relaxation measurement, they are shifted by 90° ⁴⁷. The spin-locking
55
56 measurements were performed at five different irradiation powers characterized by
57
58
59
60

1
2
3
4 corresponding angular velocities ω_1 of ^2H nuclei (*i.e.* 8.7×10^4 , 5.1×10^4 , 2.0×10^4 , 1.3×10^4 , and
5
6 0.63×10^4 $\text{rad}\cdot\text{s}^{-1}$). As explained in the SI, under the simultaneous influence of irradiation
7
8 power ω_1 and residual static quadrupolar coupling (ω_Q), three different angular velocities,
9
10 noted k_1 , k_2 and k_3 , monitor the time evolution of the coherences of spin $I=1$ nuclei
11
12 (see Eqs S5-6 in the SI). Figure 10 illustrates the range of angular velocities that can be
13
14 potentially probed by our spin-locking relaxation measurements. As explained in the SI, the
15
16 first eigen-mode (*i.e.* k_1) is probed thanks to the contribution of the quadrupolar relaxation
17
18 mechanism (see Eq. S4a in the SI), covering here a limited dynamical range (see Figure 10).
19
20 Hopefully, the next two eigen-modes (*i.e.* k_2 and k_3) are probed by the hetero-nuclear dipolar
21
22 relaxation mechanism (see Eq. S5a in the SI) extending by three decades the probed
23
24 dynamical range (see Figure 10) while the initial range of angular velocities ω_1 covers only
25
26 one decade between (8.7×10^4 and 0.63×10^4) $\text{rad}\cdot\text{s}^{-1}$, as detailed above. Since both quadrupolar
27
28 and heteronuclear dipolar relaxation mechanisms have nearly the same order of magnitude
29
30 (see Section III.2), the experimental conditions are adequate to successfully investigate the
31
32 whole dynamical range displayed in Figure 10
33
34
35
36
37
38
39
40
41

42 Figure 10 and 11

43
44
45
46 Figure 11 illustrates the free induction decays typically recorded for both $T_{1\rho}$ and $T_{2\rho}$
47
48 spin-locking relaxation measurements in addition with their Fourier Transforms, better
49
50 exhibiting the frequency domain covered by these spin-locking relaxation measurements.
51
52 Both set of figures also display the results of numerical modeling of the time evolution of the
53
54 coherences (see Eqs S14 and S16 in the SI) during each step of the pulse sequences displayed
55
56 in Figure 9. These numerical results were obtained by using the set of parameters displayed in
57
58 Section III.2 and fitting a single empirical law describing the dispersion of the spectral
59
60

1
2
3
4 densities. The resulting law, displayed in Figure 10, is used to determine the characteristic
5
6 angular velocity ω_c below which all spectral densities are equal to their value at zero angular
7
8 velocity and above which they all decrease according to the same logarithmic law. Figure 10
9
10 first illustrates the theoretical spectral density used to fit the spin-locking relaxation
11
12 measurements displayed in figures 11a-h. As noted in the insert, this unique normalized
13
14 spectral density (see the black line in Figure 10) is used to determine the six spectral densities
15
16 monitoring the contributions from the quadrupolar and hetero nuclear dipolar couplings
17
18 (see the SI). The only crucial parameter is the characteristic angular velocity (noted ω_c)
19
20 corresponding to transition between the low frequency plateau and the high frequency
21
22 logarithmic decrease of the spectral density. In addition, Figure 10 also displays the
23
24 distribution laws of the angular velocities respectively probed during the performed spin-
25
26 locking relaxation measurements by the quadrupolar coupling, leading to the set of (k_1)
27
28 angular velocities and the hetero nuclear dipolar coupling, leading to the set of (k_2, k_3)
29
30 angular velocities. While the quadrupolar relaxation mechanism probes here angular
31
32 velocities varying between 10^5 and 3×10^5 rad/s, the hetero nuclear dipolar relaxation
33
34 mechanism covers a broad dynamical range varying between 10^2 and 2×10^5 rad/s. Since the
35
36 characteristic angular velocity is localized in the middle of that probed dynamical range, we
37
38 may be quite confident on the reliability of the extracted parameter (ω_c). The evaluation of
39
40 the average residence time of the water molecules confined within the clay interlayer
41
42 ($\tau_c = 1/\omega_c$) is the main purpose of that NMR study.
43
44
45
46
47
48
49
50
51
52
53

54 As displayed in Figure 11, fair agreement with experimental data is obtained by setting
55
56 the characteristic angular velocity ω_c equal to 10^4 rad s^{-1} (see Figure 10). Such procedure was
57
58 already used successfully to analyze ^2H spin-locking relaxation measurements of heavy water
59
60

1
2
3
4 confined within various clay sediments²⁵⁻²⁹. As shown by numerical simulations of water
5
6 relaxation induced by diffusion within clay interlamellar space²⁷, the characteristic time τ_c
7
8 defined by the inverse of the characteristic angular velocity $\tau_c = 1/\omega_c$ corresponds to the
9
10 average residence time of the confined water molecules. It may be used to evaluate the order
11
12 of magnitude of the self-diffusion coefficient of the confined water molecules, with $\tau_c = 10^{-4}$ s,
13
14 according to the relationship:
15
16
17
18
19

$$D \approx \frac{L^2}{2 \tau_c} = \frac{(3 \pm 1)^2 \times 10^{-14} \text{ m}^2}{2 \times 10^{-4} \text{ s}} = (6 \pm 3) \times 10^{-10} \text{ m}^2 \cdot \text{s}^{-1} \quad (3)$$

20
21
22
23
24
25 where L is the average size of the clay platelets (see Section II.1). Whatever the
26
27 dimensionality of the diffusion space, the self-diffusion coefficient is defined by the ratio
28
29 between the mean squared displacement and the diffusion time, leading to Eq. 3. For
30
31 2D diffusion one would rather expect:
32
33
34
35

$$D = \lim_{\tau \rightarrow \infty} \frac{(dx)^2 + (dy)^2}{4 d\tau} \quad (4)$$

36
37
38
39
40
41 However, Eq. 3 simply formulates the derivation of the order of magnitude of the self-
42
43 diffusion coefficient, in agreement with previous numerical simulations of Brownian
44
45 Dynamics²⁶. The resulting mobility is compatible with experimental data obtained by
46
47 QENS^{13,20,48,49} for water molecules confined within clay sediments under equivalent
48
49 conditions. The water mobility of the confined water molecules evaluated by Equation 3 fully
50
51 matches the radial component of the water self-diffusion tensor evaluated by MD simulations
52
53 ($D \approx (6.6 \pm 0.5) \times 10^{-10} \text{ m}^2/\text{s}$).
54
55
56
57
58
59
60

1
2
3
4 This water mobility determined by ^2H NMR spin-locking relaxometry is at least ten times
5
6 larger than the cesium mobility previously evaluated by ^{133}Cs NMR spin-locking
7
8 relaxometry³⁰ within the same sediment of fluoro-hectorite. Such a large increase of water
9
10 mobility by reference to ionic mobility is not surprising because the interaction of water
11
12 dipole with the charged interlayer is significantly smaller than the strong electrostatic
13
14 coupling between negatively charged clay surface and the neutralizing counterions. The water
15
16 mobility reported here by ^2H spin-locking relaxometry is twice as large as the value
17
18 previously measured by QENS²⁰ and ^2H spin-locking relaxometry²⁸ within either fluorinated
19
20 or hydroxylated hectorite neutralized by sodium counterions and under the same hydration
21
22 condition, *i.e.* when confined water molecules form a single hydration layer with a
23
24 characteristic period of 12.2 \AA^{33} . That difference originates from the significant increase of
25
26 the ion/water interactions after the exchange of cesium counterions by the smaller⁵⁰ and more
27
28 hydrophilic⁵¹ sodium cations.
29
30
31
32
33
34

35 **IV. Conclusions**

36
37
38 ^2H NMR was successfully used to quantify the influence of confinement on the
39
40 structural and dynamical properties of water molecules physisorbed within dense clay
41
42 sediments. ^2H NMR spectroscopy was first used to probe the influence of the chemical
43
44 composition of the clay surface on the ordering of water molecules pertaining to the first
45
46 hydration layer in the clay interlamellar space. Replacing polar hydroxides groups at the
47
48 surface of clay platelets by hydrophobic fluorine atoms significantly enhances the residual
49
50 quadrupolar coupling felt by the confined water molecules, quantifying the increase of water
51
52 ordering at contact with the clay surface. Multi-quantum ^2H NMR relaxation measurements
53
54 were then performed to determine the contributions of the quadrupolar and hetero-nuclear
55
56 dipolar couplings responsible for the NMR relaxation of the confined water molecules. The
57
58
59
60

1
2
3
4 high sensitivity of the time evolution of the T_{21}^{IR} coherence on the residual quadrupolar
5
6 coupling was also exploited to determine the distribution of the individual clay directors
7
8 within the macroscopic sediment. Finally, spin-locking relaxometry measurements were used
9
10 to determine the average residence time of water molecules confined within the interlamellar
11
12 space of the clay platelets, leading to reliable estimate of the impact of confinement on the
13
14 decrease of water mobility. This extraction of dynamical information on the mobility of
15
16 confined water molecules requires the use of some theoretical formalism able to numerically
17
18 describe the time evolution of the various spin states probed by the ^2H nuclei during each step
19
20 of the pulse sequences used to perform the required NMR measurements. While this study
21
22 focuses on the clay/water interface, it may be extended to other interfacial systems, including
23
24 zeolitic porous networks, membranes or liquid crystals where information about the
25
26 dynamical properties of confined fluids is of prime importance.
27
28
29
30
31

32 33 **Associated Content**

34
35
36 **Supporting Information.** Full details concerning the NMR relaxation theory and necessary
37
38 to understand the data analysis are provided in the Supporting Information (SI).
39
40

41 42 **Author Information**

43 44 **Corresponding Authors:**

45
46 *E-mail: delville@cnrs-orleans.fr (A.D.) and porion@cnrs-orleans.fr (P.P.).
47
48
49

50 51 **ORCID:**

52 Patrice Porion: 0000-0003-4380-5995
53
54

55 56 **Notes:**

57 The authors declare no competing financial interest.
58
59
60

Acknowledgments

The DSX360 Bruker spectrometer used for that study was purchased thanks to grants from Région Centre (France). We acknowledge the contribution from the NEEDS interdisciplinary project (MIPOR, MULTIDYN). We cordially thank Dr Joseph Breu (Institut für Anorganische Chemie der Universität Regensburg) for providing Hectorite clay sample. The authors are grateful to José C. Gomes and Santiago Braley for their help in the design and the machining of the glass cell.

References

- (1) Israelachvili, J. N. *Intermolecular and Surface Forces*; Academic Press: New York, 1985.
- (2) Bowers, G. M.; Singer, J. W.; Bish, D. L.; Kirkpatrick, R. J. Alkali Metal and H₂O Dynamics at the Smectite/Water Interface. *J. Phys. Chem. C* **2011**, *115*, 23395-23407.
- (3) Henderson, D. *Fundamentals of Inhomogeneous Fluids*; M. Dekker: New York, 1992.
- (4) Cygan, R. T.; Greathouse, J. A.; Heinz, H.; Kalinichev, A. G. Molecular Models and Simulations of Layered Materials. *J. Mater. Chem.* **2009**, *19*, 2470-2481.
- (5) Jobbagy, M.; Iyi, N. Interplay of Charge Density and Relative Humidity on the Structure of Nitrate Layered Double Hydroxides. *J. Phys. Chem. C* **2010**, *114*, 18153-18158.
- (6) Lee, S. S.; Fenter, P.; Park, C.; Sturchio, N. C.; Nagy, K. L. Hydrated Cation Speciation at the Muscovite (001)-Water Interface. *Langmuir* **2010**, *26*, 16647-16651.
- (7) Ferrage, E.; Sakharov, B. A.; Michot, L. J.; Delville, A.; Bauer, A.; Lanson, B.; Grangeon, S.; Frapper, G.; Jiménez-Ruiz, M.; Cuello, G. J. Hydration Properties and Interlayer Organization of Water and Ions in Synthetic Na-Smectite with Tetrahedral Layer Charge. Part 2. Toward a Precise Coupling between Molecular Simulations and Diffraction Data. *J. Phys. Chem. C* **2011**, *115*, 1867-1881.
- (8) Boily, J. F. Water Structure and Hydrogen Bonding at Goethite/Water Interfaces: Implications for Proton Affinities. *J. Phys. Chem. C* **2012**, *116*, 4714-4724.
- (9) Ho, T. A.; Argyris, D.; Cole, D. R.; Striolo, A. Aqueous NaCl and CsCl Solutions Confined in Crystalline Slit-Shaped Silica Nanopores of Varying Degree of Protonation. *Langmuir* **2012**, *28*, 1256-1266.
- (10) Briman, I. M.; Rébiscoul, D.; Diat, O.; Zanotti, J. M.; Jollivet, P.; Barboux, P.; Gin, S. Impact of Pore Size and Pore Surface Composition on the Dynamics of Confined Water in Highly Ordered Porous Silica. *J. Phys. Chem. C* **2012**, *116*, 7021-7028.
- (11) Gates, W. P.; Bordallo, H. N.; Aldridge, L. P.; Seydel, T.; Jacobsen, H.; Marry, V.; Churchman, G. J. Neutron Time-of-Flight Quantification of Water Desorption Isotherms of Montmorillonite. *J. Phys. Chem. C* **2012**, *116*, 5558-5570.
- (12) Malani, A.; Ayappa, K. G. Relaxation and Jump Dynamics of Water at the Mica Interface. *J. Chem. Phys.* **2012**, *136*, 194701.
- (13) Michot, L. J.; Ferrage, E.; Jiménez-Ruiz, M.; Boehm, M.; Delville, A. Anisotropic Features of Water and Ion Dynamics in Synthetic Na- and Ca-Smectites with Tetrahedral Layer Charge. A Combined Quasi-Elastic Neutron-Scattering and Molecular Dynamics Simulations Study. *J. Phys. Chem. C* **2012**, *116*, 16619-16633.
- (14) *Handbook of Clay Science*; 1st ed.; Bergaya, F.; Theng, B. K. G.; Lagaly, G., Eds.; Elsevier: Amsterdam, 2006; Vol. 1.
- (15) Jiménez-Ruiz, M.; Ferrage, E.; Delville, A.; Michot, L. J. Anisotropy on the Collective Dynamics of Water Confined in Swelling Clay Minerals. *J. Phys. Chem. A* **2012**, *116*, 2379-2387.
- (16) Cygan, R. T.; Daemen, L. L.; Ilgen, A. G.; Krumhansl, J. L.; Nenoff, T. M. Inelastic Neutron Scattering and Molecular Simulation of the Dynamics of Interlayer Water in Smectite Clay Minerals. *J. Phys. Chem. C* **2015**, *119*, 28005-28019.

- 1
2
3
4 (17) Michot, L. J.; Ferrage, E.; Delville, A.; Jiménez-Ruiz, M. Influence of Layer Charge,
5 Hydration State and Cation Nature on the Collective Dynamics of Interlayer Water in
6 Synthetic Swelling Clay Minerals. *Appl. Clay Sci.* **2016**, *119*, 375-384.
7
8 (18) Jiménez-Ruiz, M.; Ferrage, E.; Blanchard, M.; Fernandez-Castanon, J.; Delville, A.;
9 Johnson, M. R.; Michot, L. J. Combination of Inelastic Neutron Scattering Experiments
10 and Ab Initio Quantum Calculations for the Study of the Hydration Properties of
11 Oriented Saponites. *J. Phys. Chem. C* **2017**, *121*, 5029–5040.
12
13 (19) Michot, L. J.; Delville, A.; Humbert, B.; Plazanet, M.; Levitz, P. Diffusion of Water in a
14 Synthetic Clay with Tetrahedral Charges by Combined Neutron Time-of-Flight
15 Measurements and Molecular Dynamics Simulations. *J. Phys. Chem. C* **2007**, *111*, 9818-
16 9831.
17
18 (20) Marry, V.; Dubois, E.; Malikova, N.; Durand-Vidal, S.; Longeville, S.; Breu, J. Water
19 Dynamics in Hectorite Clays: Influence of Temperature Studied by Coupling Neutron
20 Spin Echo and Molecular Dynamics. *Environ. Sci. Technol.* **2011**, *45*, 2850-2855.
21
22 (21) Callaghan, P. T. *Principles of Nuclear Magnetic Resonance Microscopy*; Clarendon
23 Press: Oxford, 1991.
24
25 (22) Kimmich, R.; Fatkullin, N. Self-Diffusion Studies by Intra- and Inter-Molecular Spin-
26 Lattice Relaxometry Using Field-Cycling: Liquids, Plastic Crystals, Porous Media, and
27 Polymer Segments. *Prog. Nucl. Magn. Reson. Spectrosc.* **2017**, *101*, 18-50.
28
29 (23) Korb, J. P.; Delville, A.; Xu, S.; Demeulenaere, G.; Costa, P.; Jonas, J. Relative Role of
30 Surface Interactions and Topological Effects in Nuclear Magnetic Resonance of
31 Confined Liquids. *J. Chem. Phys.* **1994**, *101*, 7074-7081.
32
33 (24) Korb, J.-P. Multiscale Nuclear Magnetic Relaxation Dispersion of Complex Liquids in
34 Bulk and Confinement. *Prog. Nucl. Magn. Reson. Spectrosc.* **2018**, *104*, 12-55.
35
36 (25) Porion, P.; Michot, L. J.; Faugère, A. M.; Delville, A. Structural and Dynamical
37 Properties of the Water Molecules Confined in Dense Clay Sediments: A Study
38 Combining ^2H NMR Spectroscopy and Multiscale Numerical Modeling. *J. Phys. Chem.*
39 *C* **2007**, *111*, 5441-5453.
40
41 (26) Porion, P.; Michot, L. J.; Faugère, A. M.; Delville, A. Influence of Confinement on the
42 Long-Range Mobility of Water Molecules within Clay Aggregates: A ^2H NMR Analysis
43 Using Spin-Locking Relaxation Rates. *J. Phys. Chem. C* **2007**, *111*, 13117-13128.
44
45 (27) Porion, P.; Michot, L. J.; Warmont, F.; Faugère, A. M.; Delville, A. Long-Time
46 Dynamics of Confined Water Molecules Probed by ^2H NMR Multiquanta Relaxometry:
47 An Application to Dense Clay Sediments. *J. Phys. Chem. C* **2012**, *116*, 17682-17697.
48
49 (28) Porion, P.; Faugère, A. M.; Delville, A. Multiscale Water Dynamics within Dense Clay
50 Sediments Probed by ^2H Multiquanta NMR Relaxometry and Two-Time Stimulated
51 Echo NMR Spectroscopy. *J. Phys. Chem. C* **2013**, *117*, 26119-26134.
52
53 (29) Porion, P.; Faugère, A. M.; Delville, A. Structural and Dynamical Properties of Water
54 Molecules Confined within Clay Sediments Probed by Deuterium NMR Spectroscopy,
55 Multiquanta Relaxometry, and Two-Time Stimulated Echo Attenuation. *J. Phys. Chem.*
56 *C* **2014**, *118*, 20429-20444.
57
58 (30) Porion, P.; Warmont, F.; Faugère, A. M.; Rollet, A.-L.; Dubois, E.; Marry, V.; Michot, L.
59 J.; Delville, A. ^{133}Cs Nuclear Magnetic Resonance Relaxometry as a Probe of the
60

- 1
2
3
4 Mobility of Cesium Cations Confined within Dense Clay Sediments. *J. Phys. Chem. C*
5 **2015**, *119*, 15360-15372.
6
7 (31) Kimmich, R.; Anoardo, E. Field-Cycling NMR Relaxometry. *Prog. Nucl. Magn. Reson.*
8 *Spectrosc.* **2004**, *44*, 257-320.
9
10 (32) Dazas, B.; Lanson, B.; Breu, J.; Robert, J.-L.; Pelletier, M.; Ferrage, E. Smectite
11 Fluorination and Its Impact on Interlayer Water Content and Structure: A Way to Fine
12 Tune the Hydrophilicity of Clay Surfaces ? *Microporous Mesoporous Mater.* **2013**, *181*,
13 233-247.
14
15 (33) Dazas, B.; Lanson, B.; Delville, A.; Robert, J.-L.; Komarneni, S.; Michot, L. J.; Ferrage,
16 E. Influence of Tetrahedral Layer Charge on the Organization of Interlayer Water and
17 Ions in Synthetic Na-Saturated Smectites. *J. Phys. Chem. C* **2015**, *119*, 4158-4172.
18
19 (34) Breu, J.; Seidl, W.; Stoll, A. J.; Lange, K. G.; Probst, T. U. Charge Homogeneity in
20 Synthetic Fluorohectorite. *Chem. Mater.* **2001**, *13*, 4213-4220.
21
22 (35) Neilson, G. W.; Enderby, J. E. Chapter 7. Neutron and X-Ray Diffraction Studies of
23 Concentrated Aqueous Electrolyte Solutions. *Annu. Rep. Prog. Chem., Sect. C, Phys.*
24 *Chem.* **1979**, *76*, 185-220.
25
26 (36) Müller, N.; Bodenhausen, G.; Ernst, R. R. Relaxation-Induced Violations of Coherence
27 Transfer Selection Rules in Nuclear Magnetic Resonance. *J. Magn. Reson.* **1987**, *75*,
28 297-334.
29
30 (37) van der Maarel, J. R. C. The Relaxation Dynamics of Spin I=1 Nuclei with a Static
31 Quadrupolar Coupling and a Radio-Frequency Field. *J. Chem. Phys.* **1993**, *99*, 5646-
32 5653.
33
34 (38) Plimpton, S. Fast Parallel Algorithms for Short-Range Molecular Dynamics. *J. Comput.*
35 *Phys.* **1995**, *117*, 1-19.
36
37 (39) Cygan, R. T.; Liang, J. J.; Kalinichev, A. G. Molecular Models of Hydroxide,
38 Oxyhydroxide, and Clay Phases and the Development of a General Force Field. *J. Phys.*
39 *Chem. B* **2004**, *108*, 1255-1266.
40
41 (40) Abascal, J. L. F.; Vega, C. A General Purpose Model for the Condensed Phases of
42 Water: TIP4P/2005. *J. Chem. Phys.* **2005**, *123*, 234505.
43
44 (41) Reddy, U. V.; Bowers, G. M.; Loganathan, N.; Bowden, M.; Yazaydin, A. O.;
45 Kirkpatrick, R. J. Water Structure and Dynamics in Smectites: X-Ray Diffraction and ²H
46 NMR Spectroscopy of Mg-, Ca-, Sr-, Na-, Cs-, and Pb-Hectorite. *J. Phys. Chem. C*
47 **2016**, *120*, 8863-8876.
48
49 (42) Woessner, D. E. Nuclear Transfer Effects in Nuclear Magnetic Resonance Pulse
50 Experiments. *J. Chem. Phys.* **1961**, *35*, 41-48.
51
52 (43) Fukushima, E.; Roeder, S. B. W. *Experimental Pulse NMR: A Nuts and Bolts Approach*;
53 Addison-Wesley: Reading, MA, 1981.
54
55 (44) Petit, D.; Korb, J. P.; Delville, A.; Grandjean, J.; Laszlo, P. Theory of Nuclear Spin
56 Relaxation in Heterogeneous Media and Application to the Cross Correlation between
57 Quadrupolar and Dipolar Fluctuations of Deuterons in Clay Gels. *J. Magn. Reson.* **1992**,
58 *96*, 252-279.
59
60

- 1
2
3
4 (45) Barbara, T. M.; Vold, R. R.; Vold, R. L. A Determination of Individual Spectral
5 Densities in a Smectic Liquid-Crystal from Angle Dependent Nuclear Spin Relaxation
6 Measurements. *J. Chem. Phys.* **1983**, *79*, 6338-6340.
7
8 (46) Hwang, D. W.; Jhao, W.-J.; Hwang, L.-P. ^2H $T_{2\rho}$ Relaxation Dynamics and Double-
9 Quantum Filtered NMR Studies. *J. Magn. Reson.* **2005**, *172*, 214-221.
10
11 (47) Blicharski, J. S. Nuclear Magnetic Relaxation in Rotating Frame. *Acta Phys. Pol.* **1972**,
12 *A41*, 223-236.
13
14 (48) Malikova, N.; Cadène, A.; Dubois, E.; Marry, V.; Durand-Vidal, S.; Turq, P.; Breu, J.;
15 Longeville, S.; Zanotti, J. M. Water Diffusion in a Synthetic Hectorite Clay Studied by
16 Quasi-Elastic Neutron Scattering. *J. Phys. Chem. C* **2007**, *111*, 17603-17611.
17
18 (49) Marry, V.; Dubois, E.; Malikova, N.; Breu, J.; Haussler, W. Anisotropy of Water
19 Dynamics in Clays: Insights from Molecular Simulations for Experimental QENS
20 Analysis. *J. Phys. Chem. C* **2013**, *117*, 15106-15115.
21
22 (50) Enderby, J. E.; Neilson, G. W. The Structure of Electrolyte Solutions. *Rep. Prog. Phys.*
23 **1981**, *44*, 593-653.
24
25 (51) Rashin, A. A.; Honig, B. Reevaluation of the Born Model of Ion Hydration. *J. Phys.*
26 *Chem.* **1985**, *89*, 5588-5593.
27
28
29
30
31
32
33
34
35
36
37
38
39
40
41
42
43
44
45
46
47
48
49
50
51
52
53
54
55
56
57
58
59
60

Figure 1

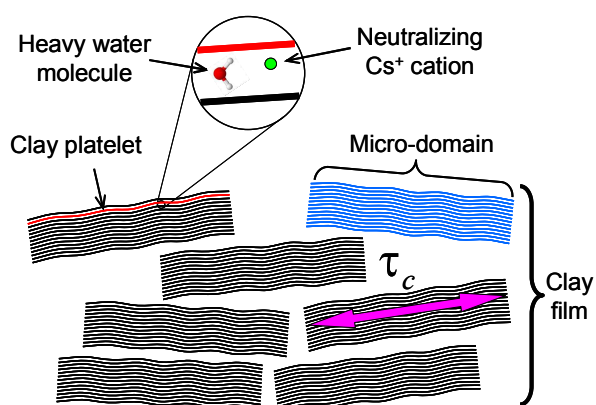


Figure 1. Schematic view of the multi-scale organization of the clay sample within the self-supporting film.

Figure 2

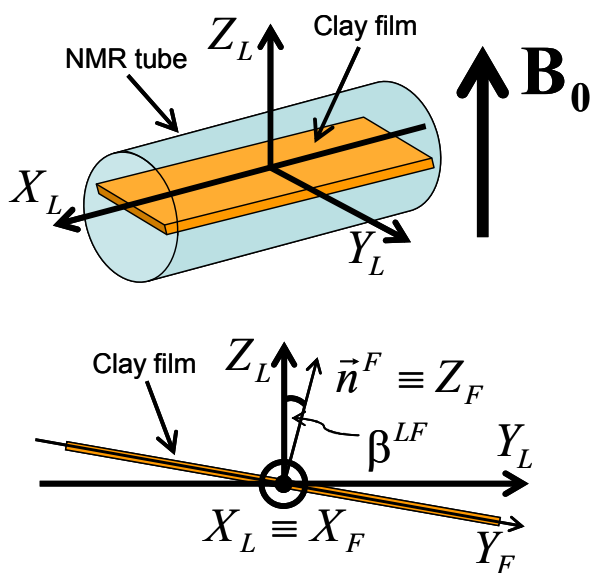


Figure 2. Schematic view of the film orientation within the NMR tube used to insert the clay sample into the detection coil within the static magnetic field \mathbf{B}_0 (see text).

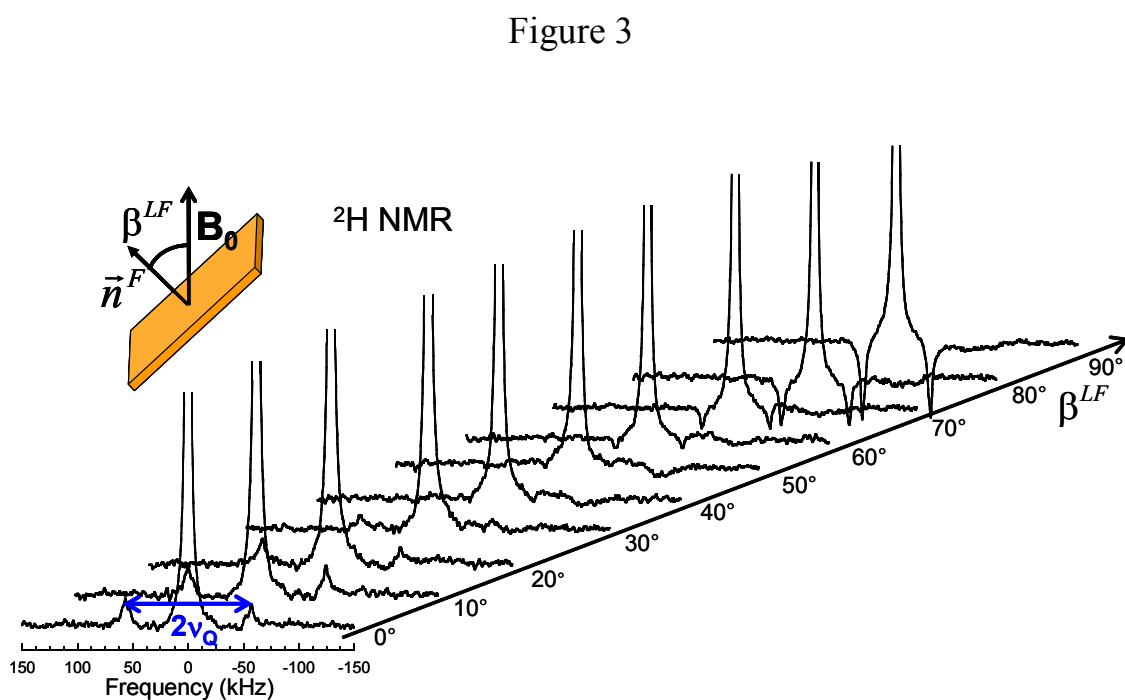


Figure 3. Variation of the ^2H NMR spectra of confined and bulk water molecules as a function of the orientation β^{LF} of the film director \vec{n}^F into the static magnetic field \mathbf{B}_0 (see text and Figure 2).

Figure 4

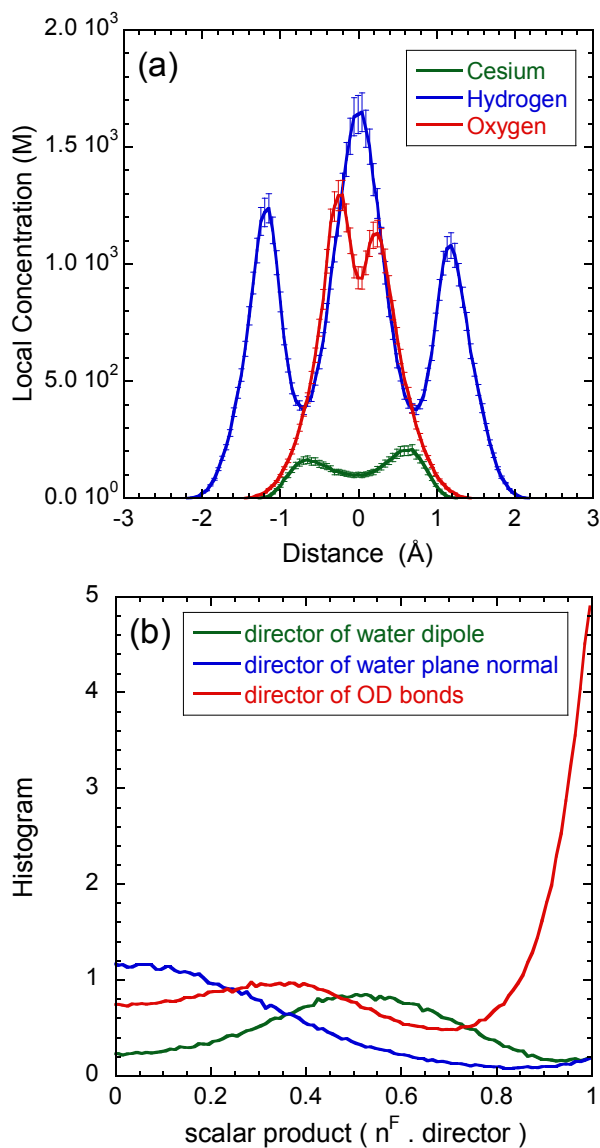


Figure 4. (a) Concentrations profiles of the neutralizing cesium cation in addition to the hydrogen and oxygen atoms of the confined water molecules. The plots are centered on the equatorial plane located at the middle of the interlamellar space. (b) Analysis of the orientation of the confined water molecules based on the distributions, by reference to the normal of the clay platelets, of three different directors attached to the water molecules and describing respectively the water dipole, the normal to the *DOD* plane and the *OD* director (see text).

Figure 5

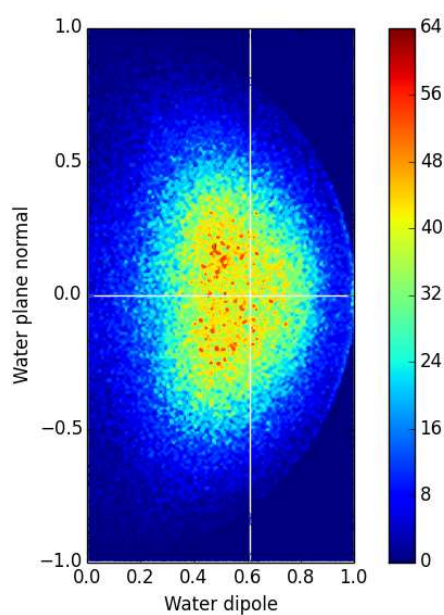


Figure 5. 3D plot illustrating the ordering of the confined water molecules characterized by the simultaneous distribution of the orientation of the water dipole and the normal to the *DOD* plane by reference to the normal of the clay platelet. Details concerning the horizontal and vertical white reference lines are given in the text.

Figure 6

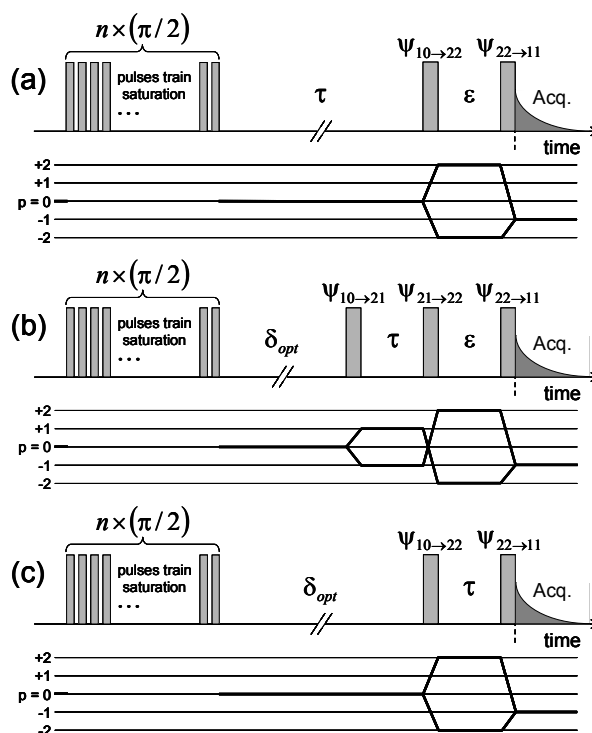


Figure 6. Pulse sequences and coherences transfer pathways used to measure (a) the relaxation rate $R_{10} = 1/T_1$ of the coherence T_{10}^{IR} by a saturation-recovery pulse sequence followed by a double-quanta filtering. The multiquanta relaxation rates (b) R_{21} and (c) R_{22} of the T_{21}^{IR} and T_{22}^{IR} coherences are respectively measured using pre-saturation pulses sequence and double-quanta filtering (see text). In all sequences, the evolution time τ is varied to sample the relaxation rates. The delay ϵ inserted between the two filtering pulses, for (a) and (b) sequences, is set equal to its minimum values (*i.e.* 5 μ s). Finally for (b) and (c) sequences, the delay δ_{opt} is set to 40 ms in order to recover the maximum magnetization from the confined water molecules and simultaneously minimizes the magnetization from the bulk water by exploiting the difference of their longitudinal relaxation rates R_{10} (see text).

Figure 7

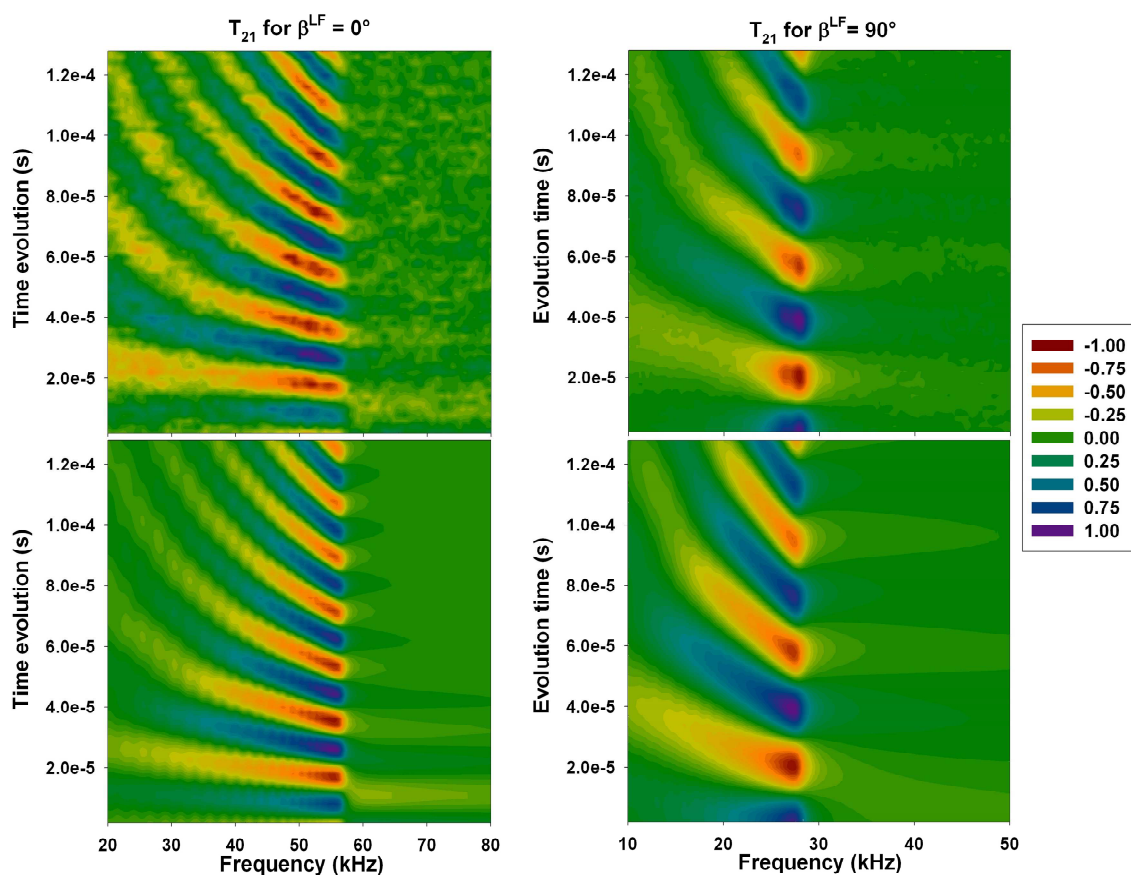


Figure 7. 3D plots illustrated the comparison between the experimental (top) and simulated (bottom) time evolution of the T_{21}^{IR} coherence performed for parallel, $\beta^{LF} = 0^\circ$ (left), and perpendicular, $\beta^{LF} = 90^\circ$ (right), orientations of the clay directors \vec{n}^F into the static magnetic field \mathbf{B}_0 (see text).

Figure 8

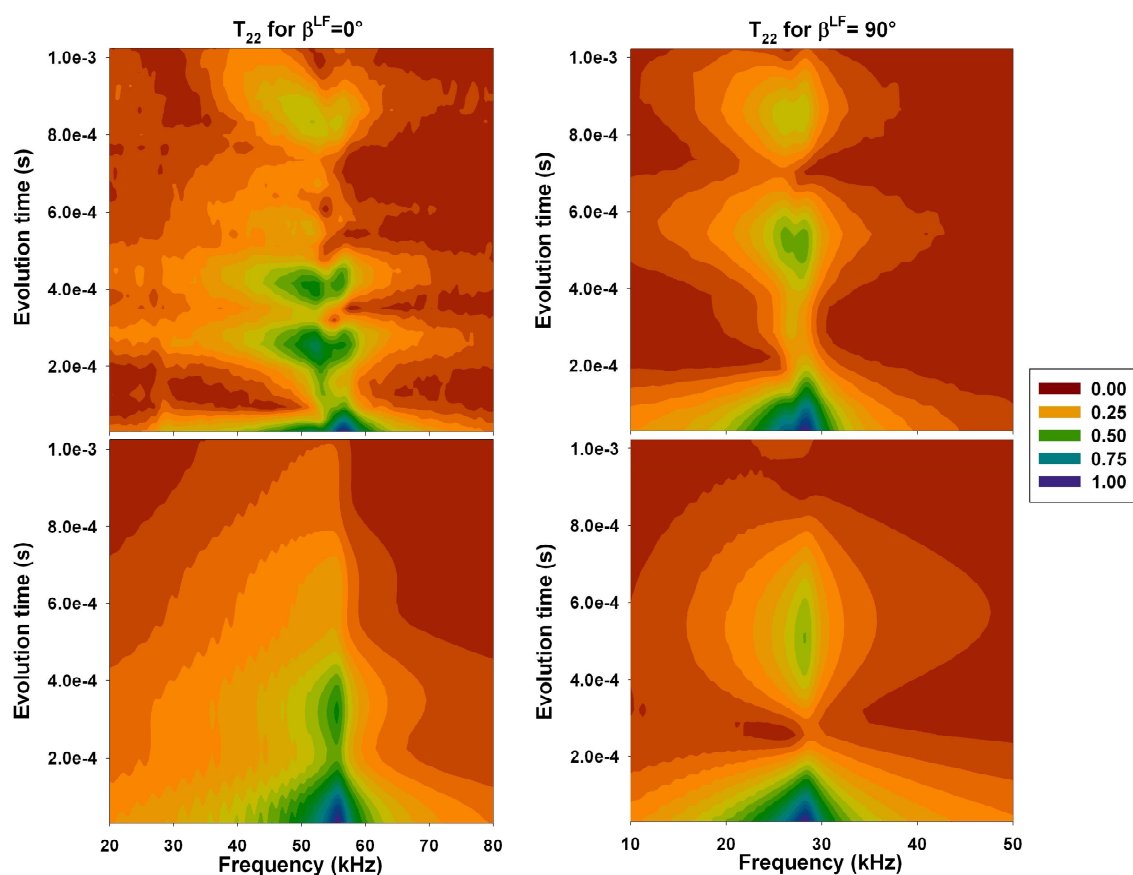


Figure 8. . 3D plots illustrated the comparison between the experimental (top) and simulated (bottom) time evolution of the T_{22}^{IR} coherence performed for parallel, $\beta^{LF} = 0^\circ$ (left), and perpendicular, $\beta^{LF} = 90^\circ$ (right), orientations of the clay directors \vec{n}^F into the static magnetic field \mathbf{B}_0 (see text).

Figure 9

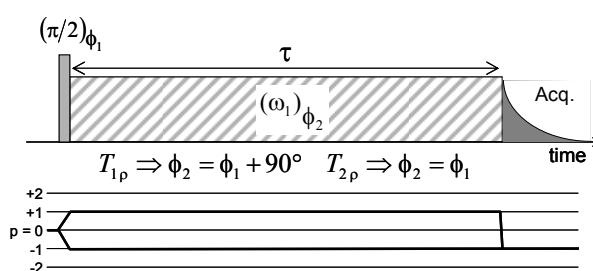


Figure 9. Pulse sequences and coherence pathways used to perform $T_{1\rho}$ and $T_{2\rho}$ spin-locking relaxometry measurements.

Figure 10

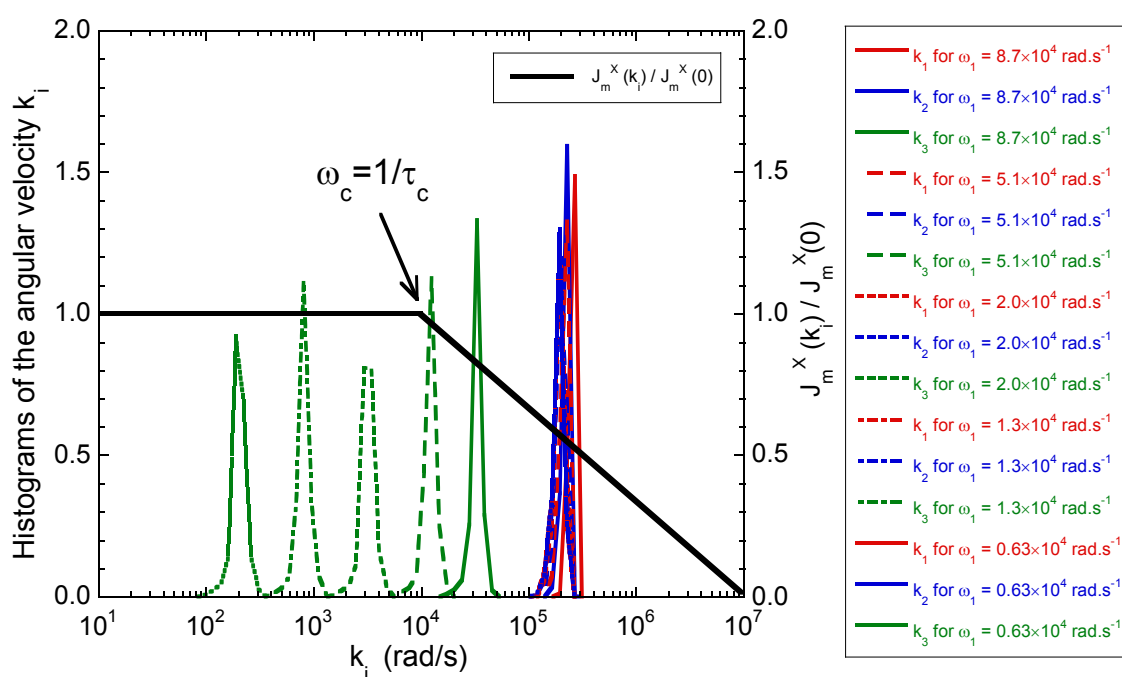


Figure 10. Distribution of the complete sets of resonance angular velocities k_i , $i \in \{1, 2, 3\}$, probed by $T_{1\rho}$ and $T_{2\rho}$ spin-locking relaxometry measurements performed at 5 different irradiating fields ω_1 , in addition to the fitted dispersion curve exhibiting the characteristic angular velocity ω_c (see text).

Figure 11

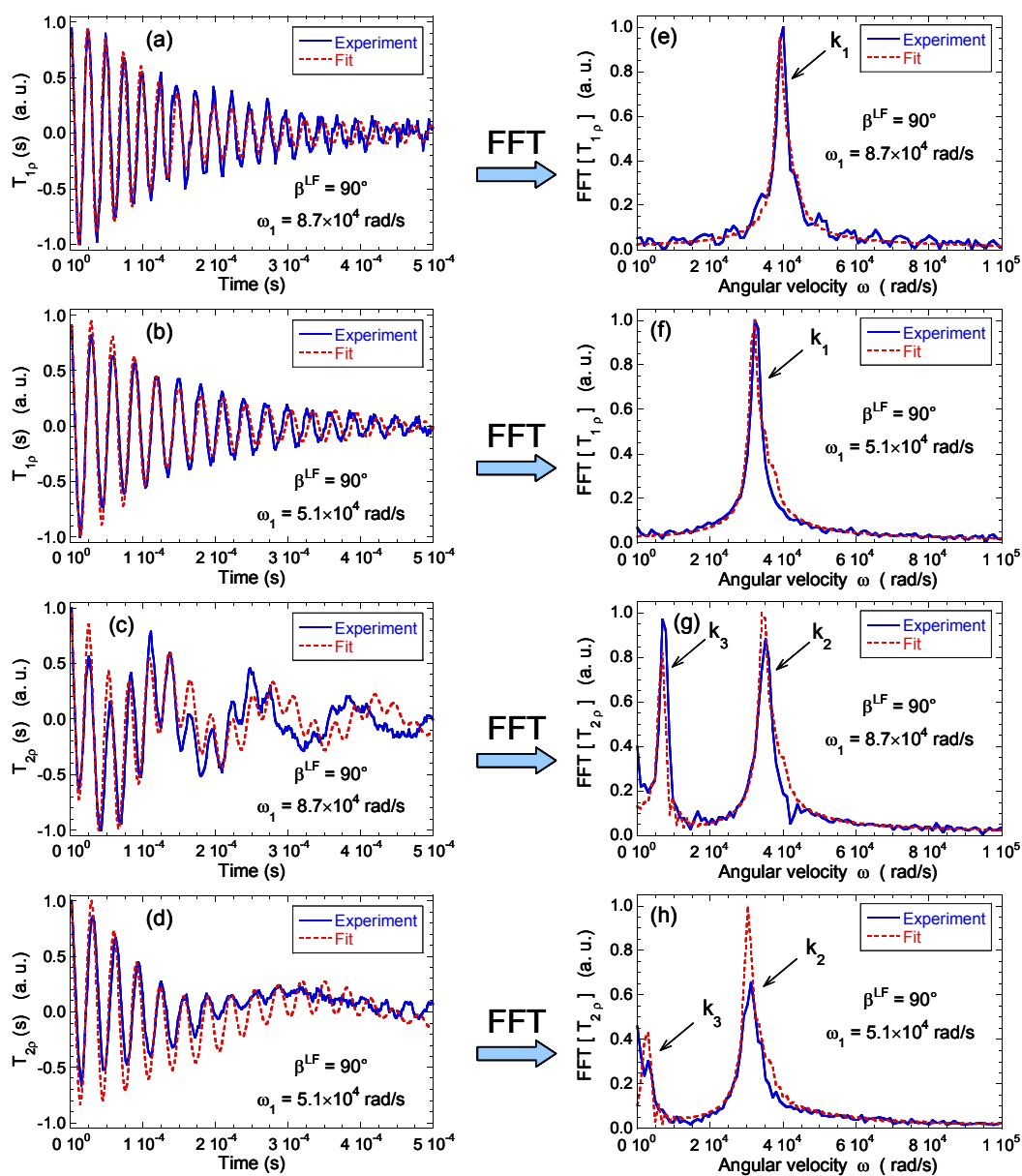


Figure 11. Comparison between measured and fitted T_{1p} (top, a-b and e-f) and T_{2p} (bottom, c-d and g-h) spin-locking relaxation rates measured at two angular velocities, $\omega_1 = 8.7 \times 10^4$ rad/s and 5.1×10^4 rad/s for $\beta^{LF} = 90^\circ$ (see text). The time evolutions of the magnetization (left, a-d) are displayed in addition to their Fourier transform (right, e-h).

Figure for Table of Contents (TOC) graphic

